2011

Physical Conditions in a Galactic Star forming region W22

Akshaya Rane
University of Kentucky, akshaya.uky@gmail.com

Recommended Citation

Rane, Akshaya, "Physical Conditions in a Galactic Star forming region W22" (2011). *University of Kentucky Master's Theses*. 158.
https://uknowledge.uky.edu/gradschool_theses/158

ABSTRACT OF THESIS

Akshaya Rane

The Graduate School
University of Kentucky
2011

Physical Conditions in a Galactic Star forming region W22

ABSTRACT OF THESIS

A thesis submitted in partial
fulfillment of the requirements for
the degree of Master of Science in
the College of Arts and Sciences at
the University of Kentucky

By
Akshaya Rane
Lexington, Kentucky

Director: Dr. Thomas Troland, Professor of Physics
Lexington, Kentucky 2011

ABSTRACT OF THESIS

Physical Conditions in a Galactic Star forming region W22

This document describes study of an active star forming region in our galaxy (the Milky Way)known as W22. Physical conditions in these regions can help us in understanding star formation processes in the universe and hence the structure and evolution of the universe. Zeeman effect measurements in 18 cm OH absorption line were carried out in order to estimate the line of sight magnetic field strength in the molecular cloud associated with this star forming region. Other physical parameters such as hydrogen column density, optical depth, critical magnetic field were also determined from these measurements. The region was mapped at 18 cm and the distribution of molecular gas within this star forming complex was described.

KEYWORDS: Molecular clouds, magnetic fields, spectral lines

Author's signature: Akshaya Rane

Date: September 30, 2011

Physical Conditions in a Galactic Star forming region W22

By
Akshaya Rane

Director of Thesis: Thomas Troland

Director of Graduate Studies: Dr.Joseph Brill

Date: September 30, 2011

RULES FOR THE USE OF THESES

Name	Date

THESIS

Akshaya Rane

The Graduate School
University of Kentucky
2011

Physical Conditions in a Galactic Star forming region W22

THESIS

A thesis submitted in partial
fulfillment of the requirements for
the degree of Master of Science in
the College of Arts and Sciences at
the University of Kentucky

By
Akshaya Rane
Lexington, Kentucky

Director: Dr. Thomas Troland, Professor of Physics
Lexington, Kentucky 2011

TABLE OF CONTENTS

LIST OF FIGURES

LIST OF TABLES

Chapter 1 Introduction

The luminous matter in the universe is composed mainly of stars. Therefore, understanding star formation is essential to understanding the structure and evolution of galaxies and the universe. However, there is also matter between the stars, Interstellar Material (ISM). This matter is composed of gas and dust and is distributed throughout our Galaxy and others. Approximately 99% of the mass of ISM is in the form of gas, and the remaining 1% is dust. The most abundant element in the ISM is hydrogen, accounting for almost 90% of it by number, 9% is helium. Much less than 1% of atoms in the ISM are heavier than hydrogen and helium and are referred to as "metals" or "heavy elements" in astronomy.

The hydrogen in ISM exists in multiple phases, distinguished by whether it is ionized H^+, atomic H^0 or molecular H_2. In the coldest and densest regions of ISM, hydrogen is primarily in molecular form. These regions are called molecular clouds. The molecules in these regions survive because they are shielded from dissociating stellar ultraviolet (uv) radiation by dust absorption. In this shielded environment, temperatures are very low, only about $10 - 20$ K. The number density n in these regions is also high (by interstellar standards) and typically ranges from $n = 10^2 - 10^6\ cm^{-3}$. (For comparison, the average density in the ISM is about 1 cm^{-3}.) Molecular clouds are surrounded by less dense envelopes of atomic gas. In these envelopes, hydrogen is dissociated into atomic form by stellar uv radiation, but the energy from the radiation is not enough to ionize H. Typical number densities of these H^0 regions range from $0.2 - 50$ atoms cm^{-3}, and temperatures are 50 K to 5000 K. Regions of ionized hydrogen H^+ are observed around hot young stars where far-uv stellar radiation ionizes the atomic hydrogen. Ionizing stellar photons must have energies greater than the ionization potential (13.6 eV) of H from its ground state ($n = 1$). Therefore, the photons have $\lambda < 92$ nm. H^+ regions have typical temperatures of 10,000 K. They are most prominent near O and B type stars since these hot stars produce copious quantities of ionizing photons. ISM near such hot stars typically exists in layers in which H is in different phases. Closest to the stars lies H^+, ionized by stellar photons with $\lambda < 92$ nm. Energy conservation ensures that nearly all of the excess photon energy (energy beyond the H ionization energy)becomes kinetic energy of the new free electrons. Collisions between these hot photoelectrons, and between electrons and ions, thermalize the ionized gas and gradually bring it into local thermodynamic equilibrium (LTE). Consequently, the thermalized electrons have a Maxwellian energy distribution. Beyond this layer lies the H^0 within which H-ionizing photons have been extinguished, but longer wavelength stellar uv radiation is capable of dissociating H_2 and other molecules. Furthest from the star lies the layer of H_2. Dust absorption in this layer has reduced the stellar radiation field to negligible intensity so that H_2 and trace molecules such as CO can survive. The neutral (i.e. non H-ionized) regions of these layers, where significant stellar radiation exists, are sometimes called Photon Dominated Regions (PDRs). The PDR includes the H^0 layer and the near portion of the H_2 layer from which stellar radiation has not been completely absorbed by dust.

Within the PDR, stellar radiation drives the chemical and physical properties of the ISM. Beyond the PDR, deep inside the molecular cloud, starlight is irrelevant to the ISM.

Although interstellar dust accounts for only 1% of ISM, it is important since it absorbs optical (and shorter) wavelengths, preventing direct observation of starlight through much of the Galaxy. More importantly, dust largely determines the physics of PDR regions near hot stars. Dust grains are irregular in shape and are typically one micron in size. They are primarily composed of heavy elements (carbon and silicates). Red giant stars that have evolved off the main sequence and known to eject much of their envelope into the interstellar space are a major source of dust grains in ISM.

As reviewed by Larson in 2003, observational studies of galaxies show that the spiral arms contain concentrations of hot, luminous young stars and associated glowing clouds of H^+. Molecular clouds are also concentrated in the spiral arms. This spatial association of young stars, H^+ regions and molecular clouds in spiral arms is no coincidence. The young stars have recently formed from the molecular clouds. Moreover, the ionizing radiation from these hot stars is in the process of ionizing what remains of the molecular clouds, and this radiation will help to destroy them.

Molecular clouds in galaxies have highly irregular structures and complex shapes. The irregular boundaries of molecular clouds have fractal-like shapes resembling those of surfaces in turbulent flows, suggesting that their shapes may be created by turbulence. Most of the molecular ISM is in the form of giant molecular clouds (GMCs) with masses of $\sim 10^5 - 10^6 M_{\odot}$, diameters $\sim$ 100 pc and average densities $< n_{H_2} >\sim 10^2$ atoms cm^{-3} (Larson 94, Williams and Blitz 1994). A nearby example in our Galaxy is the Orion Molecular Cloud at a distance of about 500 pc. Stars have recently formed from this GMC. Among the hottest of them are the O stars of the Orion Trapezium Cluster. Far-uv radiation from these hot stars has ionized the front face of the Orion Molecular Cloud and given rise to the famous Orion Nebula H^+ region.

Chapter 2 Life Cycle of Molecular Clouds

Studies of formation and evolution of the MCs are essential because they provide insight into the earliest stages in the process of star formation and also the dynamics of interstellar medium. Larson has reviewed this subject in 1994. The MCs could either be formed due to large-scale gravitational instabilities in galaxies that can collect gas into large concentrations or else by random collisions and coalescence of smaller clouds. Formation mechanisms for GMCs are still rather poorly understood, and they are the subject of ongoing observational and theoretical research.

2.1 Formation and Destruction of Molecular Clouds

Despite this uncertainty about formation mechanisms, some general conclusions can be drawn about formation timescales for GMCs. The star forming rate in our Galaxy is estimated to be $\sim 3M_{\odot}$/year. However, star formation is known to be quite inefficient. That is, only a small fraction of the mass of a GMC, perhaps 2%, actually goes into stars (Larson 1994). Given this inefficiency, we expect that $\sim 150M_{\odot}$/year of ISM is converted into molecular clouds. The total amount of ISM in our Galaxy is about $5 \times 10^9 M_{\odot}$, so the average time required to collect gas into a GMC is ~ 30 Myr (Larson 1994). The formation, internal evolution and destruction may all go on simultaneously in different parts of a star forming complex.
There are several mechanisms responsible for destruction of the molecular clouds. These mechanisms lead to the inefficiency of star formation. One mechanism is ionization by hot stars. Once a fraction of clouds mass is converted into stars, much of the remaining ISM is ionized by the newly formed stars. The H^+, owing to its sudden rise in temperature (by about two orders of magnitude), is over-pressured relative to the surrounding ISM. Therefore the gas expands at the speed of sound and dissipates into the surrounding low-density medium. A second destruction mechanism is stellar winds which inject significant mechanical energy into molecular clouds. Both ionized (H^+) and neutral (H^0, H_2) ISM are predicted to be dispersed by stellar winds at velocities of order 10 km/s. Moreover, ISM is observed to be receding from some young clusters with velocities of this order. Therefore, stellar winds appear to be important in dissipating molecular clouds, and they are likely to be a major contributor to the observed turbulent motions in the interstellar medium. Likewise, supernovae from the most massive (and shortest-lived) stars formed in molecular clouds will inject mechanical energy into the clouds. The cycle of cloud formation and destruction is eventually closed when the debris from old star forming clouds becomes the raw material for building new molecular clouds by the large-scale gravitational instability effects or other processes.

2.2 Cloud Balance and Flux Freezing

Stars form via gravitational collapse of clouds of ISM. Moreover, gravitational collapse is most likely in regions where densities are highest (strengthening the role of gravity) and temperatures are lowest (weakening the effects of internal pressure). These conditions are best met in molecular clouds. Various triggers have been proposed for pushing molecular clouds into gravitational instability, leading to collapse and eventual star formation. According to a review by Larson (2003), these triggers include collisions of GMCs and shock waves from nearby supernovae. Either process can lead to compression of the cloud, hence, to rising density and gravitational collapse. Once a molecular cloud becomes gravitationally unstable, it should collapse in the free fall time given by,

$$t_{ff} = \sqrt{\frac{3\pi}{32G\rho}} sec \tag{2.1}$$

(Crutcher 2007)
where ρ is the average density of the cloud. For a typical average cloud density corresponding to $n = fewtimes \times 10^3\ cm^{-3}$,$t_{ff} \sim 10^6$ years.
If the cloud collapses in free fall time to form stars, then the lifetime of a cloud will be very short compared to the estimated time $\approx 30 \times 10^6$ years for molecular cloud formation (see previous section). Also, in the case of such a short lifetime, the expected rate of star formation would be much higher ($\approx$ 3 orders of magnitude) than the observed rate of $3M_{\odot}$/year. Clearly, GMCs are not all in a state of free fall! The long lifetimes of GMCs compared to the free fall time implies that there are support mechanisms preventing free fall gravitational collapse. The magnetic field may be one such mechanism if magnetic fields in the clouds are sufficiently strong.
The possible relevance of magnetic fields to supporting molecular clouds rests on some simple physical principles. Although ISM is essentially neutral in H^0 and H_2 regions, there exists a small fraction of charged particles in either phase. The ionization fraction is typically 10^{-4} or less, often much less. The ions come either from starlight ionization of carbon (the first ionization potential of C is 11.3 eV, less than that for H) or else from cosmic ray ionization. Cosmic rays alone are thought to lead to a very small fractional ionization, and they are only relevant deep inside molecular clouds where C-ionizing starlight is heavily absorbed. Also, the ISM is weakly magnetized, the average magnetic field strength in the Galaxy is about $3\mu G$. As a result of the magnetic field, the motion of charged particles is affected by the Lorentz force perpendicular to both the velocity of the particle v and the magnetic field B and is given by,

$$\vec{F}_{Lorentz} = \frac{q}{c}(\vec{v} \times \vec{B}) \tag{2.2}$$

Here q is the charge of the particle and c is the speed of light.
If this is the total force on the particle then from Newtons second law, one can get

$$\vec{F}_{net} = \vec{F}_{Lorentz} = m\frac{dv}{dt} = \frac{q}{mc}(\vec{v} \times \vec{B}) \tag{2.3}$$

If the velocity of the particle is $\parallel toB$ then,

$$\frac{dv}{dt} = 0 \tag{2.4}$$

If $v \perp B$ then for a homogeneous B,

$$\frac{dv}{dt} = \frac{qvB}{mc} \tag{2.5}$$

From equations (2.4) and (2.5), it can be seen that the magnitude of velocity remains constant; i.e. the particle performs uniform circular motion with a radius r called as gyro radius. Hence, the particle traveling perpendicular to the magnetic field circles around magnetic field lines with acceleration,

$$a = \frac{qvB}{mc} \tag{2.6}$$

$$Since, \qquad a = r\omega^2, \qquad v = r\omega \Rightarrow \omega = \frac{qB}{mc} \tag{2.7}$$

where ω is called the gyrofrequency or Larmor frequency of charged particle.
A simple calculation using the above formula for a proton in a magnetic field of $3\mu G$ gives a gyro-radius of about 30 km. Here we have taken as a velocity the thermal velocity of a proton at $100K$. This radius is very small relative to any interstellar dimension; therefore, the motion of charged particles in the ISM is tightly coupled to the interstellar magnetic field B_{ISM}.
The neutral particles are not directly affected by B_{ISM}. However, the neutral particles are well coupled to the ions through ion-neutral collisions as long as the fractional ionization does not become extremely low. Therefore, the neutral particles (H^0 , H_2) are well coupled to the magnetic field, an effect called *flux freezing*. In such a circumstance, motions of a magnetized cloud will drag the magnetic field lines along with the gas. Also, if a magnetized cloud begins to collapse gravitationally, flux freezing insures that the magnetic field lines are drawn in along with the gas. That is, both field strength and gas density increase. The rising field strength implies rising magnetic pressure which can provide support to the cloud against its own gravitation.

2.3 Importance of Magnetic Fields and Ambipolar Diffusion

If the magnetic field is strong enough, it can support the cloud against gravitational collapse. In order to find out how strong the field must be to prevent collapse, the gravitational energy of the cloud is equated to the magnetic energy. The gravitational energy for a spherical cloud is given by,

$$E_g = \frac{3}{5}a\frac{GM^2}{R} \tag{2.8}$$

where $a \approx 1$ is a constant depending on the density distribution of the cloud. For a uniform density cloud, $a = 1$. For a centrally condensed cloud, a is somewhat larger.

The magnetic energy for a spherical cloud of radius R is given by,

$$E_B = b\frac{B^2R^3}{3} \tag{2.9}$$

where $b \approx 1$ is a constant accounting for magnetic gradient effects, that is, for details of the magnetic field geometry. The value of b has been estimated from numerical models of self-gravitating clouds. By setting $E_g = E_B$, the equation is solved for the critical value of B for which the two energies are equal. This value is labeled as $B_{critical}$.

$$i.e. \qquad \frac{3}{5}a\frac{GM^2}{R} = \frac{B^2_{critical}R^3}{3} \tag{2.10}$$

$$\Rightarrow B_{critical} = \sqrt{\frac{9aGM^2}{5bR^4}} \tag{2.11}$$

Since the magnetic flux is $\Phi = BR^2$, the above relation can be written in terms of Φ as,

$$\Rightarrow \frac{M}{B_{critical}R^2} = \sqrt{\frac{5b}{9aG}} \tag{2.12}$$

Or

$$\Rightarrow \left(\frac{M}{\Phi_B}\right)_{critical} = \sqrt{\frac{5b}{9aG}} \tag{2.13}$$

This is the critical mass-to-flux ratio. Crutcher has used a parameter λ defined as,

$$\lambda \equiv \frac{\left(\frac{M}{\Phi_B}\right)}{\left(\frac{M}{\Phi_B}\right)_{critical}} \tag{2.14}$$

Depending on the value of λ, the fate of the cloud can be determined. If $\lambda > 1$ ($E_g > E_B$, $B < B_{critical}$), then the cloud is called magnetically *supercritical* and B alone cannot support a self-gravitating cloud. However, if $\lambda < 1$ ($E_g < E_B, B > B_{critical}$), then the magnetic energy exceeds the gravitational energy and the cloud is supported by B regardless of external pressure. In this case, the cloud is called magnetically *subcritical*.

Even if a molecular cloud is initially magnetically supported (i.e. magnetically subcritical), the neutral particles coupled to the ions will gradually diffuse toward the cloud center due to gravitation. This process is analogous to dust particles gradually falling toward the ground on Earth (following the gravity vector) despite numerous collisions with air molecules. The diffusion of neutral particles through the magnetic field lines in the molecular cloud is called *ambipolar diffusion*. It has the effect of increasing the mass near the center of the cloud without increasing the field strength (since the field lines remain fixed). Hence, λ gradually increases on an ambipolar diffusion time scale. Regions near the center of the cloud that were originally magnetically subcritical eventually become supercritical. At this point, the magnetic field cannot support the central regions of the cloud, and they collapse to form stars. Under typical conditions in molecular clouds, the timescale for ambipolar diffusion is estimated to be $\sim 10^7$ years, an order of magnitude higher than t_{ff}. In short, if a molecular cloud is initially magnetically subcritical, then the timescale for its collapse toward star formation can be delayed by the magnetic field by an order of magnitude relative to the free fall time. In such a case, the expected cloud lifetimes become $\sim 10^7$ years, of the same order as the estimate of cloud lifetime presented above. (Crutcher et al 1987; Heiles et al 1993; McKee et al 1993). It can be concluded that the mass-to-flux ratios of molecular clouds must be measured in order to determine if magnetic fields play a role in their evolution and in star formation. If observational measurements should establish that $\lambda > 1$ for most molecular clouds, for example, then we will know that B_{ISM} plays little role in the clouds. In this case, other explanations will be needed to explain the apparent longevity of the clouds compared to their free fall time. Other explanations might include turbulent energy in the clouds. However, supersonic turbulent energy is rapidly dissipated in clouds via shock waves that heat the gas and lead to energy losses via radiation. Therefore, turbulent energy would need to be continuously replenished by the input of mechanical energy via stellar winds and supernovae if the clouds are to survive well past their free fall times.

Chapter 3 Observations of Star Forming Regions

3.1 Molecular Tracers

Although star forming molecular clouds are mostly made up of H_2, spectral line emission from this molecule usually cannot be observed. The H_2 molecule has no permanent electric dipole moment; therefore, electric dipole transitions are forbidden. Also, H_2 has a very small moment of inertia, so its energy levels are widely spaced. As a result, energy levels above the ground state are very sparsely populated at the low temperatures of molecular clouds, so emission lines are very weak (Shaw, et al. 2005). Fortunately, trace molecules in molecular clouds (e.g. CO and OH) have electric dipole moments and higher moments of inertia. As a result, they have easily observable spectral lines at low temperatures. Since these molecules are expected to coexist with H_2, emission and absorption lines from CO, OH and other trace molecules are used to study molecular clouds. Studies of emission and absorption by these molecules have revealed the distribution of molecular clouds in our Galaxy (e.g. Dame et al. 2001) and in other galaxies. Such studies also reveal the kinematics (line-of sight motions) of the clouds and allow for estimates to be made of gas densities, temperatures and masses of the clouds.

3.2 Zeeman Effect Observations

As discussed in section 2.3, the magnetic fields play an important role in the process of star formation. The only direct probe to measure magnetic field strengths in localized regions of the ISM is the radio frequency Zeeman effect. The Zeeman effect results from an interaction between the magnetic moment of an atom or molecule and an external magnetic field. However, only a very few atomic and molecular species in the ISM have appreciable magnetic moments. These are the atoms or molecules with net electronic angular momentum (spin or orbital). Since the gyromagnetic ratio (the ratio of magnetic dipole moment to angular momentum) of a particle is inversely proportional to the particle mass, *electronic* angular momentum is more than 10^3 times effective in generating a magnetic dipole moment than nuclear angular momentum. Unfortunately, most atoms and molecules of astrophysical interest have paired electrons and no electronic orbital angular momentum (e.g. CO). So their magnetic moments (associated with nuclear spin only) are very low, and their Zeeman effects extremely weak and undetectable. Exceptions are H^0 and OH, both have an odd number of electrons, hence, a net electronic spin angular momentum. For these species, the Zeeman effect is still weak but often detectable. The Zeeman effect in the ISM was first detected in the neutral hydrogen 21-cm absorption line by Verschuur (1969). The 1665 and 1667 MHz lines of OH are also very sensitive probes of the Zeeman splitting in molecular clouds. We have observed OH absorption line at 18 cm (1667.358 MHz) towards a source W22.

Zeeman Effect in OH Molecule and Energy Levels of OH

Zeeman effect in 18 cm transition in the OH molecule is one example of this process often observed in astronomical situations. In a diatomic molecule such as OH, three angular momenta determine the momentum coupling scheme: the electronic orbital angular momentum L, the electronic spin S, and the molecular rotation R. Since OH possesses a net electronic spin angular momentum, its ground electronic state is a $\Pi-$state, with $\Lambda = 1$ because it cannot have $\Sigma = 0$ (Λ is projection of L on rotation axis and Σ, Π, Δ are used to denote $\Lambda = 0, 1, 2$ for molecules). Because of the spin-orbit coupling, the spin angular momentum can be oriented in parallel or antiparallel directions to the orbital angular momentum, producing the splitting into ${}^{2S+1}\Pi_\Omega$ that is ${}^2\Pi_{1/2}$ and ${}^2\Pi_{3/2}$ states where Ω (J in case of atoms) $= \Lambda \pm S$. The ground state ${}^2\Pi_{3/2}$ is split due to interaction between the nuclei rotation and the unpaired electron motion around its orbit and is called Λ-*doubling*. Hyperfine interaction with the unpaired spin of the proton further split the levels into $2I + 1$ levels where I is the nuclear spin. Therefore each rotational state is split into four levels as shown in Figure 3.1, $F = \Omega \pm I$ where F is the total angular momentum.

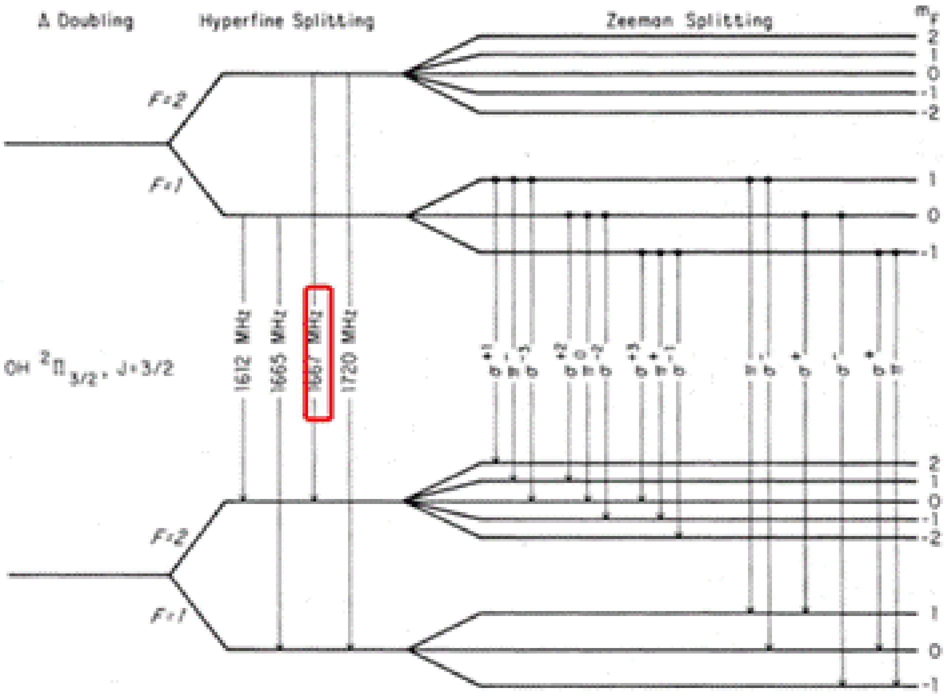

Figure 3.1: OH energy levels in ground state (Hansen 1982). Note that the transitions here show emission lines. We have observed the 1667 MHz absorption line due to the transition from F : 2 → 2.

The allowed transitions obey the selection rule $\Delta F = 0, \pm 1$ but not $\Delta F = 0$ to 0. The lines with $\Delta F = 0$ having frequencies 1665 and 1667 MHz , are called main lines. The lines with $\Delta F = \pm 1$ having frequencies 1612 and 1720 MHz , are satellite lines. At interstellar temperatures, the best observationally studied OH transmission is the

1667 MHz main line.

In the presence of external magnetic field, each level splits into magnetic sub levels with a degeneracy of $2F+1$ so these sub-levels have the same energy. The levels are denoted by magnetic quantum numbers m_F. The only transitions that are allowed are the ones obeyed by selection rule $\Delta m_F = 0, \pm 1$. All the transitions with $\Delta m_F = 0$ give π component. The transitions with $\Delta m_F = \pm 1$ are referred to as $\sigma^{\pm}$ components. In practice, the effect appears as a small frequency offset in a spectral line observed independently in opposite senses of circular polarization. The Zeeman frequency offset is usually a tiny fraction ($\approx 10^{-2}$) of the frequency width of the spectral line (Crutcher et al 2009). (The spectral line width results from the Doppler effect upon thermal and turbulent motions in the interstellar cloud.) In this limit of very small Zeeman frequency offset, the offset observed in opposite senses of circular polarization with three separate frequencies, $\nu_0 + \nu_z$, ν_z, $\nu_0 - \nu_z$, where $\nu_z = \mid BZ$ which is proportional to the line-of-sight component of the external magnetic field (B_{los}) rather than to the full magnetic field strength. However, such a small Zeeman offset can be measured by subtracting the spectral line observed in LL from that observed in RR, creating, that is, a Stokes parameter V spectral line profile. If the Zeeman effect is present, then this Stokes V profile will exhibit a scaled down replica of the derivative of the Stokes I line profile, with the amplitude of the derivative replica proportional to B_{los} (S-curve).

$$\Rightarrow V = \left[\frac{dI}{dV}\right] \nu_z cos\theta \tag{3.1}$$

where θ is the angle between the magnetic field and line of sight. Therefore,

$$B_{los} = \frac{\nu_z cos\theta}{Z} \tag{3.2}$$

can be determined. The Zeeman factor Z (in $Hz/\mu G$) is 1.96 for 1667 MHz line of OH.

3.3 Radio Recombination Lines (RRL) Observations

It is also essential to map the H^+ and H^0 regions in order to understand the physical conditions in the entire star forming complex. Most of the hydrogen in low density regions of the ISM is in neutral form and is detectable at 21 cm (ν = 1420 MHz). The magnetic interaction between the quantized electron and proton spins results in two energy levels (hyperfine splitting). When the relative spins change from parallel to antiparallel, a photon of 21 cm is emitted. In H^+ regions, heavy elements like C and O are also either singly ionized or sometimes doubly ionized depending on the energy of the photon. The free electrons in H^+ regions recombine with ions and quickly cascade to the ground state by emitting photons. Such spectral lines that are seen when an electron falls from the energy level $(n + \Delta n)$ to n are called *recombination lines*. When the difference in energy levels is very small, frequency of the radiation emitted is also small and fall into the radio spectrum.

For example, the recombination line produced by the transition between the n=110 and n=109 levels of a hydrogen atom is called the $H109_\alpha$ line where α corresponds to $\Delta n = 1$, similarly β would correspond to $\Delta n = 2$ and so on. The frequency of the photon produced by this transition from $n + \Delta n = 110$ to $n = 109$ is $\approx 5 \times 10^9$ Hz. Any singly ionized atom will have N protons and $N - 1$ electrons. Electrons recombining with such atoms orbit in the potential produced by a net charge of one proton. Therefore, the recombination-line spectra of heavier atoms are very similar to that of hydrogen.

Radiofrequency recombination lines of helium towards W22 were observed by Palmer et al. (1969) and of C92 by Chaisson et al. (1974). We have used data of $H109_\alpha$ from Wilson et al. (1970) and more recent observations of $H91_\alpha$ and $C91_\alpha$ from Quireza et al. (2006) for comparison of velocities in different regions of this star forming complex.

3.4 Column Density Observations

Spectral line observations from molecular clouds can also yield column density in cm^{-2} of molecules along the line of sight. H^+ regions associated with molecular clouds are approximated by uniform cylinders whose axis is the line of sight. The flux density is then given by,

$$S_\nu = \int_\Omega I_\nu(\theta, \phi)\, \mathrm{d}\Omega \qquad Wm^{-2}Hz^{-1} \tag{3.3}$$

I_ν is the specific intensity of the source and is independent of the distance of the source. I_ν changes only if radiation is absorbed or emitted, characterized by the equation of transfer given as,

$$\frac{dI_\nu}{ds} = -\kappa_\nu I_\nu + j_\nu \tag{3.4}$$

Where κ_ν is the absorption coefficient and j_ν is the emission coefficient.

$$dI_\nu = -\kappa_\nu I_\nu ds + j_\nu ds \tag{3.5}$$

If there is no emission, $j_\nu = 0$ and

$$\int \frac{dI}{I} = -\int \kappa_\nu ds \Rightarrow \ln \frac{I_\nu}{I_0} = -\int \kappa_\nu ds \equiv \tau_\nu \tag{3.6}$$

The quantity τ_ν is referred to as *optical depth* and it measures the exponential intensity reduction. The solution of equation (3.4) is,

$$I_\nu = \frac{j_\nu}{\kappa_\nu}(1 - e^{-\tau}) \tag{3.7}$$

As mentioned in chapter (1), most of the ISM is in thermal equilibrium, hence the specific intensity is given by the Planck's function,

$$B_\nu = \frac{2h\nu^3}{c^2} \frac{1}{e^{h\nu/kT} - 1} \tag{3.8}$$

At radio wavelengths,

$$h\nu \ll kT \Rightarrow e^{h\nu/kT} \approx \frac{h\nu}{kT} + 1 \tag{3.9}$$

Therefore,

$$B_\nu(T) = \frac{2kT\nu^2}{c^2} \Rightarrow B_\nu(T) \propto T \tag{3.10}$$

Hence in Radio astronomy, brightness of an extended source is measured by its brightness temperature T_b for which $B_\nu(T_b) = I_\nu$
Eq. (3.4) gives,

$$-\kappa_\nu I_\nu + j_\nu = 0 \Rightarrow B_\nu = j_\nu/\kappa_\nu \tag{3.11}$$

$$I_\nu(s) = I_\nu(0)e^{-\tau_\nu(s)} + B_\nu(T)[1 - e^{-\tau}] \tag{3.12}$$

$$\Rightarrow T_b(s) = T_b(0)e^{-\tau_\nu(s)} + T_{ex}[1 - e^{-\tau}] \tag{3.13}$$

T_{ex} is the excitation temperature of the cloud related to the ratio of energy level populations. For upper level u and lower level l, the number of particles n can be given using Boltzman law,

$$\frac{n_u}{n_l} = \frac{g_u}{g_l} e^{-(\Delta E/kT_{ex})} \tag{3.14}$$

Where g_u and g_l are statistical weights of the upper and lower levels and T_{ex} is the temperature at which we expect to find the system for a given ratio of populations. Note that T_{ex} is not the actual physical temperature and it cannot be measured based on absorption studies alone. I have adopted $T_{ex} = 40$ K which is used in Sarma et al. (2000) for NGC 6334.

$$\Rightarrow T_b(s) = T_{ex}[1 - e^{-\tau}] \tag{3.15}$$

For $\tau \ll 1$, $T_b = T_{ex}\tau$ and the region is called optically thin.
And $T_b = T_{ex}$ for optically thick region.
The opacity can be measured from optical depth profiles and therefore the number of particles (N(OH) for our observations) per unit area of cross-section along the line of sight can be determined using the relation,

$$\frac{N(OH)}{T_{ex}} = C \int \tau_\nu d\nu \qquad cm^{-2}K^{-1} \tag{3.16}$$

The constant $C = 2.2785 \times 10^{14}\ cm^{-2}(\text{km } s^{-1})^{-1}$ for the OH 1667 MHz line (Sarma et al. 2000). N(OH) is referred to as the column density of particles and it has units of cm^{-2}. This column density can be used to determine the proton column density assuming a standard OH abundance ratio of

$$\frac{N(H)}{N(OH)} = 2 \times 10^6 \tag{3.17}$$

(Roberts et al. 1995).
The proton column density can be determined form another relation,

$$\frac{A_v}{N(H)} = 5.3 \times 10^{22} \tag{3.18}$$

known from observations.
Where A_v is the visual extinction defined as the absorption and scattering of electromagnetic radiation by interstellar dust given by,

$$A_v = -2.5log_{10}(I/I_0) \tag{3.19}$$

It is measured in units of apparent magnitude decrease per kpc.

Chapter 4 W22 Region

4.1 Overview of W22 and its Surroundings

The radio source W22 is one giant molecular cloud where active star formation is taking place. It is located in the Sagittarius spiral arm of our galaxy. The galactic longitude of W22 is 353.2 and galactic latitude is 0.9. It is therefore near the galactic plane and in direction of galactic center. It is also identified with the diffuse emission nebula NGC 6357, RCW 131 and Sh-2 11 in the Sharpless catalogue. The nebula is a host to 3 compact HII regions in different stages of evolution. It also contains the open star cluster Pismis-24 which is responsible for ionization of the nebula.The distance to W22 was estimated to be 1.74±0.31 kpc through photometric observations (Neckel 1978, Lortet et al. 1984); however, Massey (2000) estimated the distance to be 2.56 ± 0.1 kpc based on spectroscopic study of stars within the cluster. We adopt this distance for our study.

NGC 6357 is also in close proximity to another active HII region NGC 6334, which is at the same distance and they are connected by a filamentary structure, suggesting that both regions belong to the same complex (Wang et al. 2007, Russeil et al. 2010) as shown in Figure 4.1.Compared with this region, no masers are seen in NGC 6357; only one water maser has been found (Sakellis et al. 1984). This would either indicate that no massive star formation is taking place anymore in this region (Persi et al. 1986) or the ionization front has spread over it (Healy et al. 2004).

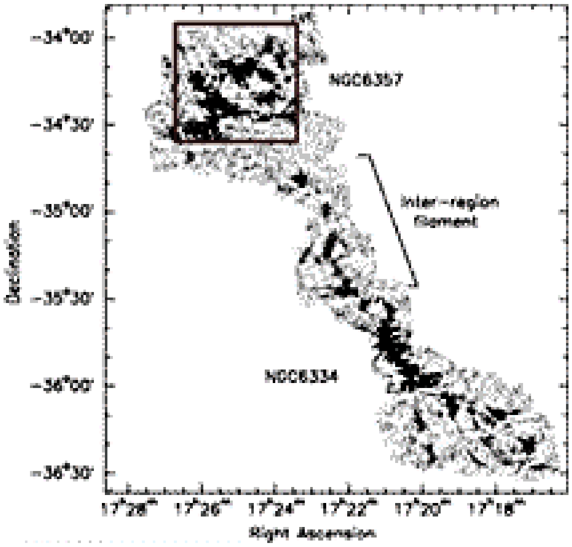

Figure 4.1: This is 1.2mm continuum emission observed by Munoz et al. (2007) with SIMBA (Russeil et al. 2010). The red box shows the region observed for current data.

4.2 Star Cluster Pismis-24

The open star cluster Pismis-24 is home to several massive stars and is located to the south of the nebula. It is been studied in optical, IR and X-rays. An extensive X-ray study of the young stars in the cluster using Chandra estimates that the cluster has $\sim$ 10000 stars, a few times richer than Orion (Wang et al. 2007). As compared to Orion, Pismis-24 is still a young cluster consisting of early type stars with some extremely massive and luminous stars, including O3.5 If (Pismis 24-1) and O3.5 IIIf (Pismis 24-17) (Walborn et al. 2002), each having masses greater than $100M_\odot$. These massive stars provide a UV photon flux of $(1.4-3.3)\times 10^{50}\ s^{-1}$ (Martins et al.2002). However, additional massive stars should be identified to explain the ionization of the gas in the whole complex Cappa et al. (2011).

4.3 Description of HII Regions in W22

A recent study of this complex based on 1.2mm data has found about 65 dense cores shown in Figure 4.1, of which 15 are more massive than $100M_\odot$ and a core with highest mass of $665M_\odot$. These dense cores have mean densities $\sim 1.7\times 10^4\ cm^{-3}$ and are likely host precursors of high-mass stars (Russeil et al 2010). Optical study also shows that the nebula is highly inhomogeneous in density (Lortet et al 1984).

The brightest and youngest HII region in NGC 6357 is $G353.2+0.9(=W22B)$ located at RA, Dec.$(J2000) = 17^h24^m48^s$, $-34^d\ 10^m\ 58^s$. W22 B lies at the northern interface between the cluster and the molecular cloud with the observed mass of ionized hydrogen $\sim 300M_\odot$. It has a sharp boundary facing the massive open cluster Pismis-24 (Figure 4.2). Most of the energy powering W22 B and its surrounding is provided by O3-O7 stars (particularly Pismis 24-1 and Pismis 24-17) emitting a powerful flux of Lyman continuum, 10^{50} UV photons s^{-1} (Bohigas et al 2004). The other HII region $G353.1+0.7(=W22A)$, located at RA, Dec.$(J2000) = 17^h25^m36^s$, $-34^d\ 22^m\ 43^s$ is an evolved region and recent studies have shown that no active star formation is seen in this region.No high density components or infrared early type stars are found in G353.2+0.7 (Felli et al. 1990). W22 A and W22 B are separated by roughly 1 pc. The general distribution of ionized and neutral gas is discussed in detail in later sections.

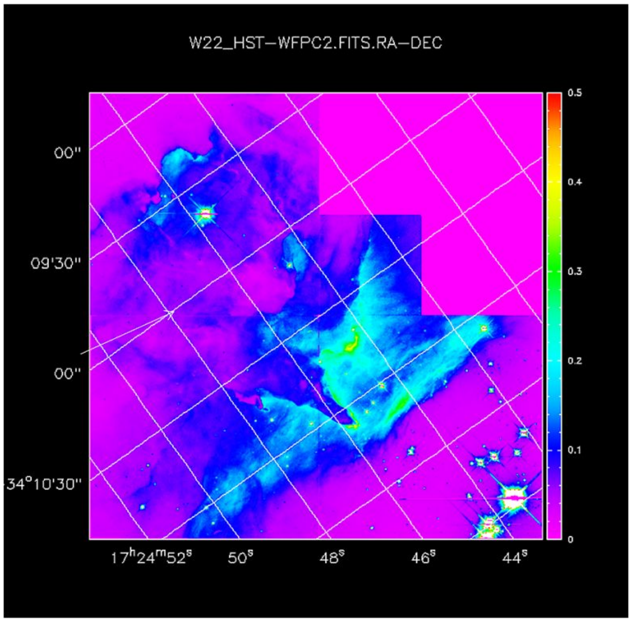

Figure 4.2: This image is taken by HST-WFPC2 camera at $0.8\mu m$. It shows some of the brightest stars of Pismis-24 and part of the molecular cloud.

Chapter 5 Observations and Data Reduction

5.1 Overview of the Very Large Array (VLA)

The Zeeman effect in molecular lines is very sensitive to measurements. Although the Zeeman studies of W22 have been done previously, they were carried out using single dish radio telescopes. The single dish radio telescopes have diffraction limitation. The diffraction of a telescope is expressed as,

$$\theta \approx \frac{\lambda}{D} \qquad (radians) \tag{5.1}$$

Where λ is the observing wavelength and D is the diameter of the antenna.
In order to deal with this diffraction limited resolution, some highly complicated techniques have been developed. These are known as arrays in which single dish elements are combined to work together to form a single telescope. The main advantages are increased resolution and increased sensitivity. In such arrays, the resolution is determined by the maximum separation between the telescopes instead of the diameter of each telescope and is referred to as the baseline length, B. The maximum separation between two antennas is the projected separation as viewed from the radio source and not the true separation on the ground. As the Earth rotates, the radio source moves across the sky during the observation and hence the effective separation between a pair of antennas (the baseline) also changes with time.
The diffraction limit with an interferometer is,

$$\theta \approx \frac{\lambda}{B} \qquad (radians) \tag{5.2}$$

The baseline length can be extended to many kilometers thereby the resolution can be increased. Interferometers can thus reveal fine details in an object. Antenna pairs with greater separations measure higher spatial frequencies, providing information about smaller angular scale features in the image. Likewise, antenna pairs with smaller separations provide information about larger angular scale features of the image.
One of the many such interferometers is the Very Large Array (VLA), operated by National Radio Astronomy Observatory (NRAO) in New Mexico. The VLA consists of 27 antennas each of 25m diameter. The array works in four different configurations (A, B, C and D) and three additional hybrid configurations (DnC, CnB, BnA) with the maximum achievable separation between antennas (baseline length) being 36 kms for A configuration; D configuration being the most compact configuration. The antennas have receivers for seven wavelength bands centered near 90, 20, 6, 3.6, 2, 1.3, 0.7 cm. These bands are commonly referred to as P, L, C, X, U, K and Q bands. The VLA antennas can tune to two different frequencies from the same wavelength band provided the frequency difference does not exceed $\sim$ 450 MHz. Right hand circular (RCP) and Left hand circular (LCP) polarizations are received for both frequencies.

Each of these four data streams is called an IF (Intermediate Frequency channel). All the observations for this project were carried out using this array.

5.2 Observations

The OH absorption data were obtained with the DnC configuration of the VLA in 1992. The important parameters of the OH observations are listed in Table 5.1. The 1667 MHz main line was observed simultaneously in both senses of circular polarization (RCP and LCP, referred to in VLA terminology as RR and LL, respectively). Simultaneous observations are possible since each VLA antenna is equipped with two independent feed and receiver systems, each sensitive to a sense of circular polarization.

Table 5.1: Observational parameters of 18 cm OH Zeeman observations of W22

Parameter	Value
Observing Date	1992 June 12-1992 June 15
Configuration	DnC
Rest frequency (MHz)	1667.359
R.A. of field center (J2000)	17 25 08.541
Decl. of field center (J2000)	-34 17 41.549
Total bandwidth (MHz)	0.19
Frequency channels per polarization	128
Channel spacing (kHz)	1.53 (-0.27 km s^{-1})
Velocity coverage	$+16.28$ km s^{-1} to -18.28 km s^{-1}
Time on source (hr)	6.8
Primary beam HPBW	27
Synthesized beam HPBW	$48.''55 \times 30.''31$
RMS noise in line channels (mJy $beam^{-1}$)	20
RMS noise in continuum (mJy $beam^{-1}$)	191
Angular to linear scale*	$1' = 0.75$ pc

*Assuming a distance of 2.56 kpc.

In an interferometric array such as the VLA, signals from each telescope are multiplied by signals from every other telescope in pairs. Since the VLA has 27 antennas, there are $n(n-1)/2 = 351$ pairs, each providing RR and LL outputs. In effect, each telescope pair is a separate interferometer operating in a mode analogous to the Young's two slit experiment in light. Multiplication of the RR signals from a telescope pair yields data for RR circular polarization, and similarly for the LL signals. Then Stokes parameter I data can be constructed from the sum RR + LL, and Stokes parameter V data can be constructed from the difference $RR - LL$. In order to investigate possible linear polarization in the data, we also multiplied RR times LL for each telescope pair creating outputs referred to in the VLA system as RL.

The RL products yield data on Stokes parameter Q. Finally, we multiplied RR times LL, the latter delayed by 90 degrees in phase to create an output known as LR. The LR products yield data on Stokes parameter U. Note that in the convention of VLA data taking and analysis, all Stokes parameters are actually reported to be average instead of their standard definitions (e.g. $I_{VLA} = 1/2(RR + LL)$). We follow this VLA convention in all figures in this manuscript. Unlike most other VLA Zeeman observations, we did not use the transfer switches in each telescope. If used, these switches invert the signal paths from the two circularly-polarized feed horns of the telescopes to the two receiver chains every few minutes. As a result, for example, signals from the RR feeds are connected to the RR receiver chains for half the observing time, and the RR feed signals are connected to the LL receiver chains for the other half. This process mitigates bandpass effects in the Stokes parameter V data. We describe our alternate approach for these data to deal with bandpass effects in the section 5.3.

5.3 Data Reduction

Data reduction for radio telescope arrays is an arduous process of many steps. The basic data from the array are a series of complex "visibilities", each is the amplitude and phase of the fringe pattern associated with a given pair of telescopes. The visibilities are the Fourier transform of the image of the astronomical source. The calibration, mapmaking, cleaning and other processing of OH data were carried out using both the Astronomical Image Processing System (AIPS) and Common Astronomy Software Applications (CASA) of the NRAO.

The first step in the reduction process is calibration of the program source visibilities using the observed visibilities of calibration sources. Since the calibration sources have known radio fluxes, and they are spatially unresolved by the telescope array, the true amplitudes of their visibilities are equal to their fluxes, and their true phases are zero. From this information, it is possible to determine the multiplicative factors that must be applied to the visibility amplitudes and determine the phase offsets that must be added to the visibility phases to convert observed visibilities of the calibration and the program sources into true (calibrated) visibilities. The sources 1328+307 ($\equiv 3C286$, $S_{1.67GHz} = 13.6$ Jy) and 1827-360 ($S_{1.67GHz} = 4.5$ Jy) were used as primary flux calibrator and phase calibrator respectively. The data were calibrated separately for RR and LL polarizations.

The calibrated visibilities are then inspected for the calibrator sources using the task UVPLT and any anomalous visibilities can be removed in a number of ways. This process is called flagging and it is done either interactively or non-interactively. A non-interactive task CLIP flags visibilities if the visibility amplitude and/or phases lie outside a specified range. There are various interactive tasks such as WIPER, TVFLG, SPFLG etc. The antenna gain amplitudes and phases derived from the calibration sources can be flagged if they do not yield the expected visibility amplitudes (i.e. source fluxes) and phases (i.e. 0) or if they do not change smoothly with time. Figure 5.1 shows an example of some bad visibility amplitude and phase in one of the calibrator sources obtained from our data. If calibrated visibilities are flagged

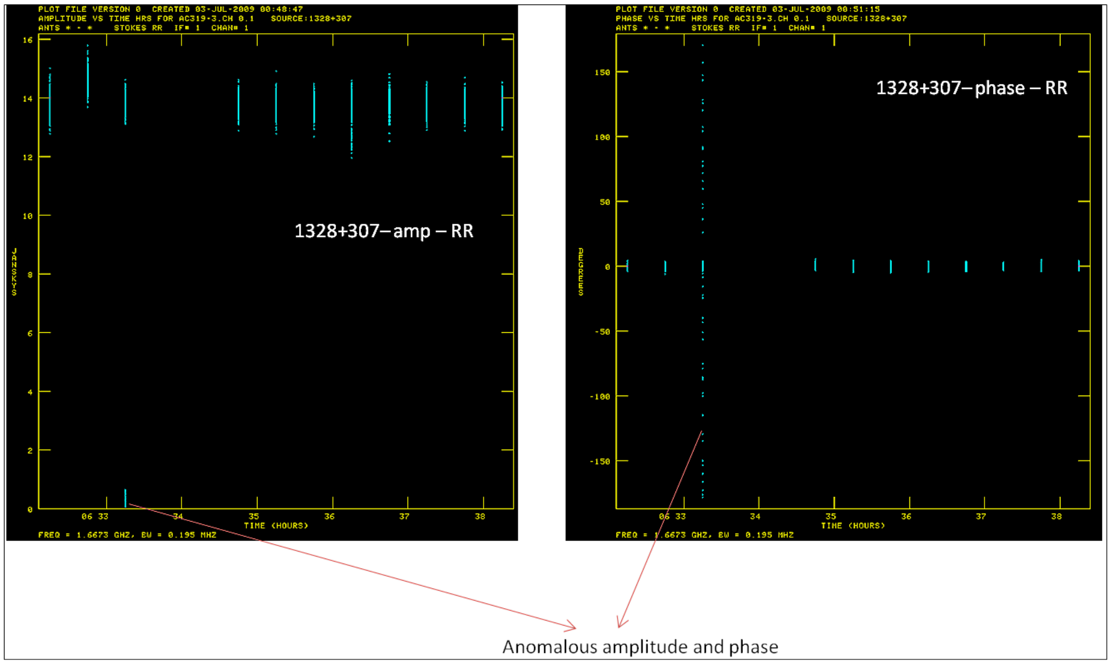

Figure 5.1: An example showing anomalous visibility amplitude and phase when plotted using the task UVPLT.

then the data are recalibrated. WIPER can be used to plot visibility amplitudes as a function of baseline in $k\lambda$ and to flag it. The data can also be edited using TVFLG which displays baseline on the x-axis, time on the y-axis and amplitude on the z-axis. SPFLG is similar to TVFLG but it shows channels on the x-axis and this task is preferred for editing spectral line data. The program source data can also be inspected and flagged using one of these tasks. Hence visibility amplitudes and phases that are bad for specific channel and/or time slot can be effectively removed. We inspected the program source data using WIPER and removed some of the bad amplitudes. Figure 5.2(a) is showing stokes I against baseline after flagging.

Some frequency channels are also severely affected due to radio frequency interference (RFI), which can be flagged too. There is a strong RFI between 1660-1700 MHz and our data being taken at 1667 MHz, there was high probability that the data are corrupted due to RFI. It can be detected if, for a range of channels, all amplitudes are exceptionally higher than at other channels. We searched for RFI with TVFLG and SPFLG. Figure 5.2(b) and 5.2(c) show one example. But we did not find any particular range of channels with high amplitudes. The data were mostly bad at a particular time or channel and were flagged accordingly.

The next step is Fourier transformation of the visibility data set into images. In practice, for the present data, there are 128 independent visibility data sets taken at adjacent frequencies. So the Fourier transformation process yields a data cube of 128 images. At any given pixel in this data cube, one may extract image brightness for all 128 channels and plot a spectral profile for that pixel. Part of the imaging process

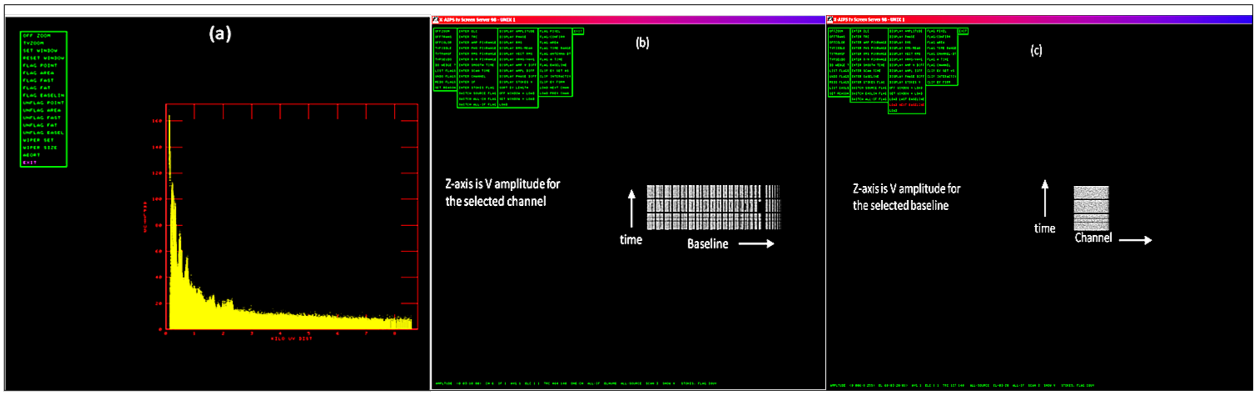

Figure 5.2: (a)This is an example showing screenshot of task WIPER for stokes I after flagging. The data can be flagged by choosing controls shown on the top left panel. (b) This is a display given by the task TVFLG. Very bright pixels can be flagged using the controls on the top left panel. (c) This is showing a display given by the task SPFLG.

is commonly referred to as "cleaning". The direct Fourier transform of visibility data normally yields an image with many artifacts, a "dirty" image. These artifacts arise because of inevitably incomplete visibility data. (Ideally, one would like to obtain visibility data for all possible separations of individual pairs of telescopes, i.e. for all possible baselines. In practice, it is impossible to do so.) The cleaning process involves an algorithm that attempts to compensate for this incompleteness of visibility information and yield images with fewer instrumental artifacts, a "clean" image. All the data (continuum and line) were imaged using natural weighting. Stokes I and V image cubes were constructed and cleaned using the CASA task CLEAN and AIPS task IMAGR. The images were then checked for inconsistencies, as described in section 7.1. Stokes V image showed a stripe pattern. Figure 5.3 shows the zoomed in stokes V image and the pattern is marked. The stripe pattern with angular separation θ is directly associated with a particular baseline as θ^{-1}. We found that baseline and flagged data within a small range. After imaging stokes V again, it was found that the stripe pattern was still present but corresponding to a different baseline.

By flagging visibilities over various ranges of baselines, we could not remove the striping pattern. Although we did not find any bad data points at those particular baselines, we could see the anomalous visibilities when we displayed data with TVFLG. Figure 5.4 clearly explains this.

It was evident that there were anomalous visibilities that created stripes in the stokes V even though they did not show up anomalously high visibility amplitudes in UVPLT.

We therefore concluded that the anomalous visibilities are either those with i)low amplitudes or ii)bad phases. In order to confirm this, phase and amplitudes were plotted against time. It was apparent that for visibilities with amplitudes less than 8 Jy, the phases were determined poorly. In particular, on long baselines, amplitudes were less than 8 Jy and phases appeared completely random as can be seen in Figure

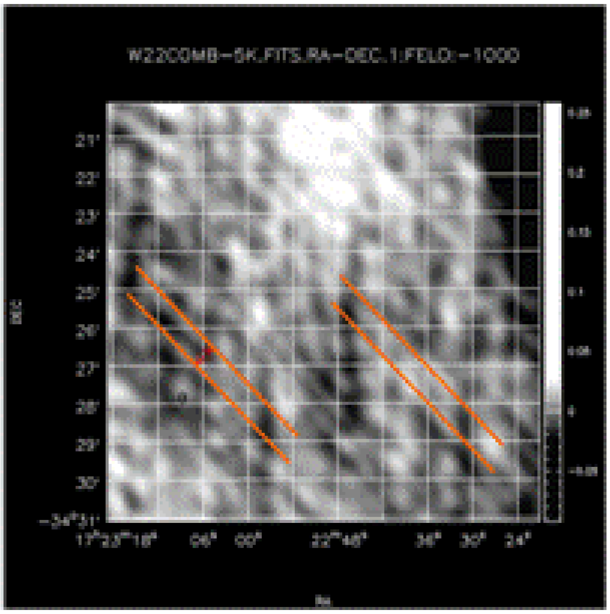

Figure 5.3: This is a stokes V image with the stripe pattern marked on it. The angular separation is θ.

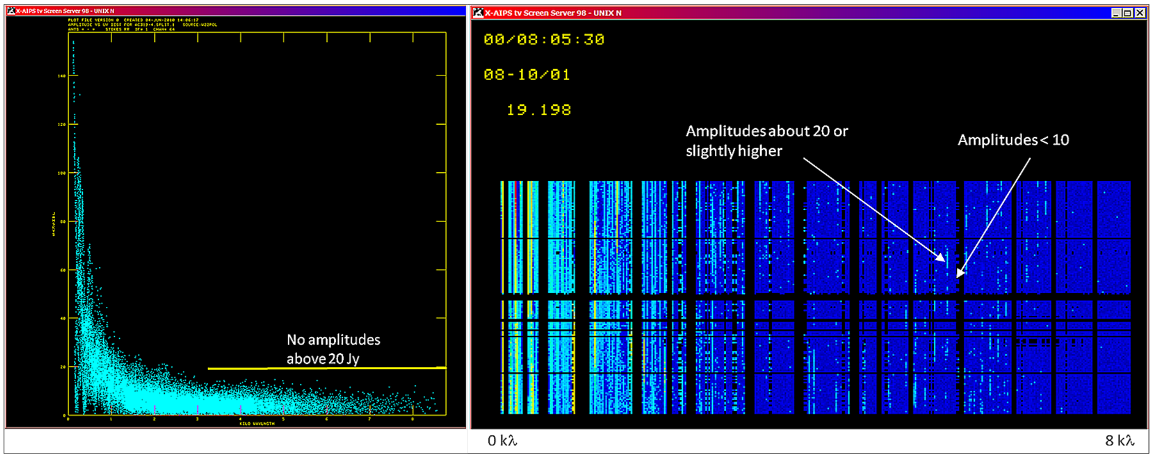

Figure 5.4: The image on the left is a plot obtained from UVPLT shows RR stokes against baseline with no amplitudes greater than 20 Jy for longer baselines. On the right is the display obtained from TVFLG showing amplitudes greater than 20 Jy at longer wavelengths.

5.5(c). After clipping visibilities below 8 Jy, the stripes were gone as shown in Figure 5.6.

Radio astronomical spectral data must, in general, be corrected for the variation in instrumental sensitivity across the bandpass, in the case of these data, across the 128 spectral channels. The function describing this variation is called the bandpass function, and it is inevitably different for RR and LL data since these data come from completely different chains of receivers. Normally, the bandpass correction is

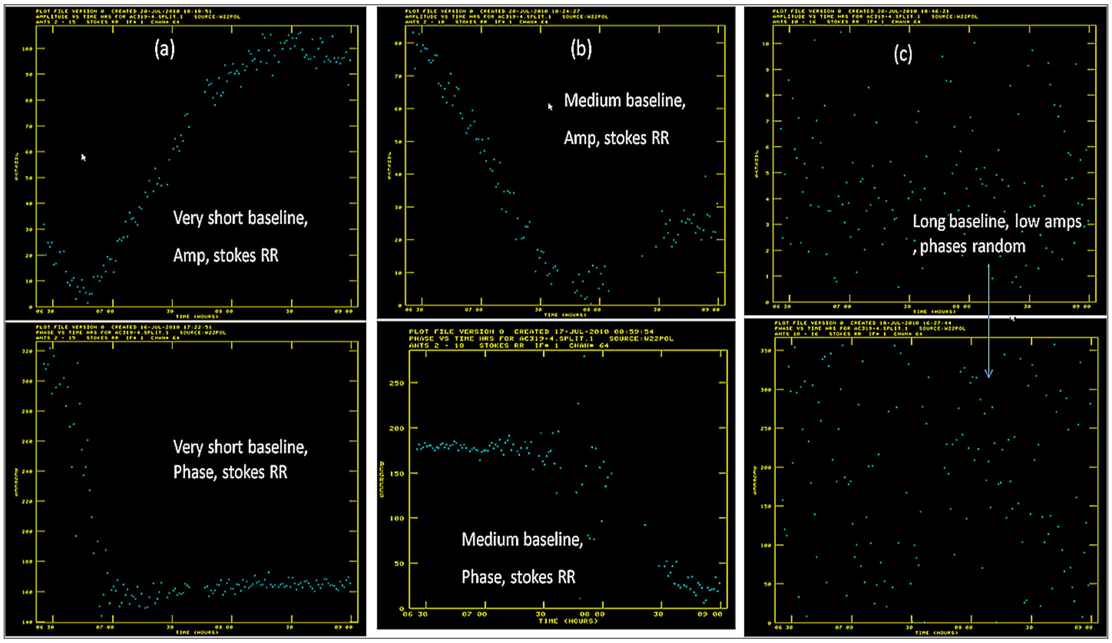

Figure 5.5: (a), (b) show a pattern when amplitude and phase is plotted as a function of time for very short baselines and medium baselines respectively. In (c), it can be seen that for long baselines the amplitudes are lower and phases are random.

achieved by dividing spectral data on the program source by spectral data on calibration sources that have no spectral lines. However, the calibration data contain noise, so the division process adds to the noise of the program source. To mitigate this noise-adding effect of bandpass correction, we used a feature of CASA in which the bandpass function obtained on the calibration sources is fit to a high order polynomial that mimics the bandpass function as closely as possible. Then the spectral data for the program source are divided by the polynomial representation of the bandpass function. Since the latter is noise free, the division adds no noise to the program source data. We used this technique with a 10^{th} order polynomial fit to obtain the best possible (i.e. least noisy) data in Stokes parameter V. Bandpass corrections were applied to both I and V data.

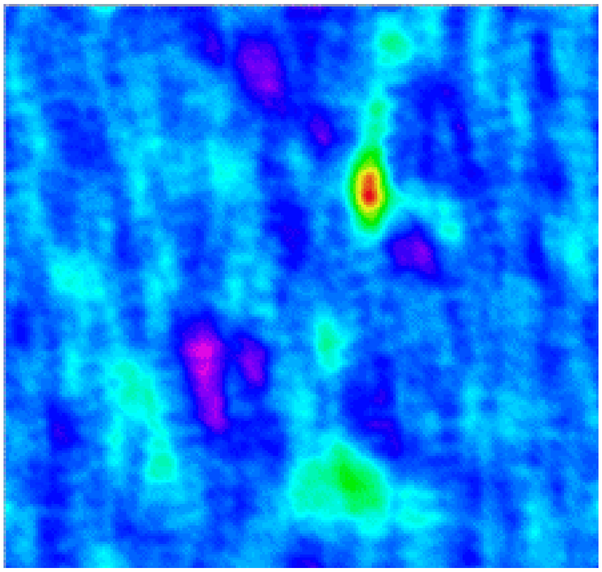

Figure 5.6: Stokes V after clipping visibilties below 8 Jy

Chapter 6 Previous Zeeman Observations Towards W22

Zeeman observations towards W22 have been carried out in 1986 using the Nancay single dish telescope in France by Kazes and Crutcher. This telescope has a collecting area of 200 by 35 meters, producing an asymmetric half-power beam diameter (primary beam) of 3.5 arc min in right ascension by 18 arc min in declination. Kazes and Crutcher searched for Zeeman splitting in both 1665 and 1667 MHz spectral lines of OH. Their results are showed in Figure 6.1. They concluded that the continuum radiation from W22 is absorbed by OH molecules in a dark cloud which is relatively near the Sun and unrelated to the H^+ region in W22. They have measured magnetic field in this cloud. This cloud is sometimes called 'Riegel-Crutcher cloud' since it was mapped by them in HI absorption in 1972. The magnetic fields measured were $-20.5 \pm 1.4\ \mu G$ for 1667 MHz and $-14.5 \pm 1.8\ \mu G$ for 1665 MHz. A search for magnetic field strengths towards W22 in a cloud associated with the H^+ region was done in a subsequent study of W22 by Crutcher, Kazes and Troland (1987). The Zeeman effect was not detected towards this position and they only determined upper limits for magnetic fields (Figure 6.2). One of the purposes of our observations was to search for Zeeman effect towards the actual cloud associated with the H^+ region using an interferometer since it provides better resolution and sensitivity which is required for Zeeman observations.

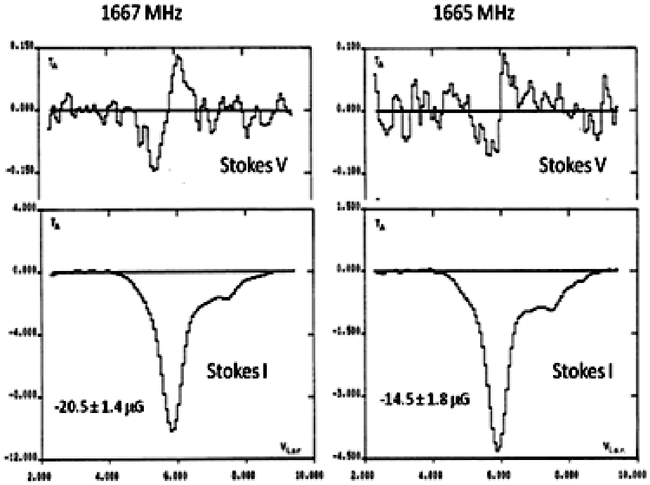

Figure 6.1: Stokes I and V profiles and measured values of magnetic fields for OH 1667 and 1665 MHz lines respectively (Kazes and Crutcher, 1986)

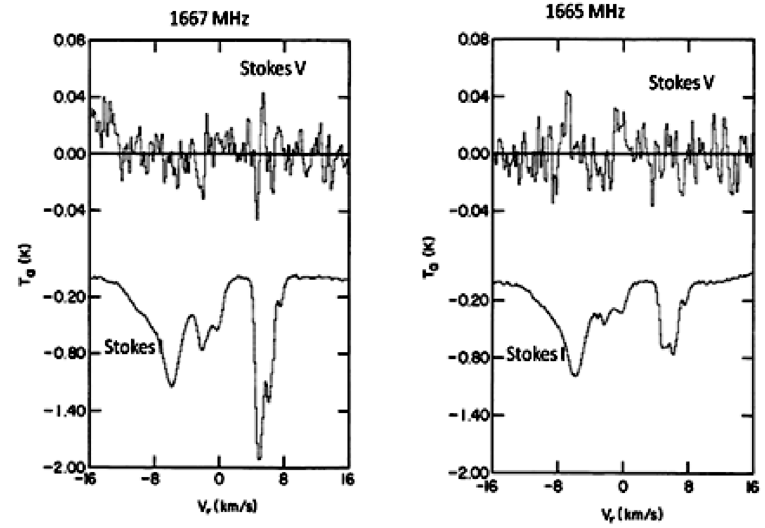

Figure 6.2: Stokes I and V profiles for OH 1667 and 1665 MHz lines respectively and note that magnetic fields are not detected (Crutcher, Kazes and Troland 1987).

Chapter 7 Results

7.1 Continuum at 18 cm

The continuum emission from an ionized hydrogen region arises due to a radiation process known as thermal Bremsstrahlung. The ionized region consists of free electrons and ions. These free electrons pass close to the ions. They are not captured but their trajectory is changed. Since the electrons are free before the interaction and remain free after emission, this emission is often referred to as free-free emission. The continuum at 18 cm arises due to this free-free emission from the ionized hydrogen region associated with W22 (Figure 7.1). It consists of two bright regions W22 A and W22 B and is centered at RA ($17^h25^m11.16^s$); DEC($-34^d17^m28.8^s$). The same region has been mapped recently at 20 cm using the VLA by Cappa et al. (2011) and the comparison of these two continuum images is shown in Figure 7.2. The circles marked show the regions reviewed in Cappa et al.(2011) and it shows the location of Pismis-24. Note that most of the bright and filamentary structures coincide at both 18 and at 20 cm. The total continuum flux at 18cm is $\sim$ 155 Jy. The continuum flux at 20 cm is 93.6 Jy. The fluxes in some filamentary structures are not consistent in the two images. The fact that the integration time in our observations is about three times than that in Cappa could account for this inconsistency.

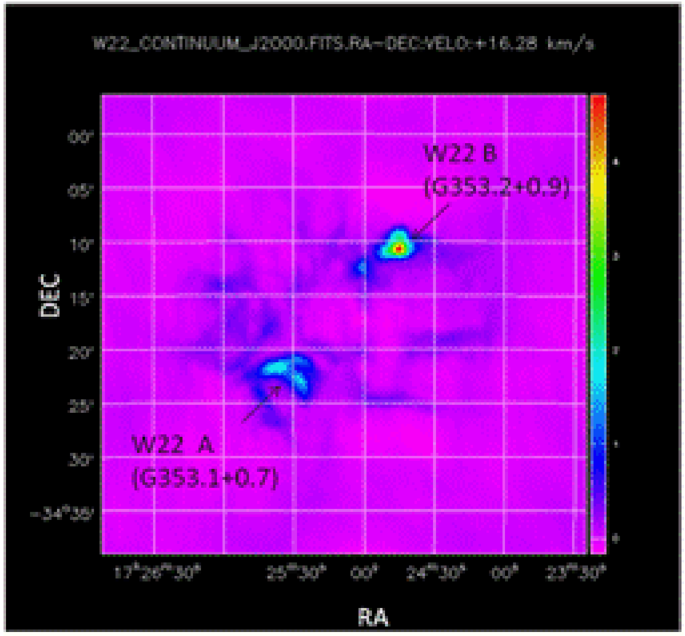

Figure 7.1: VLA continuum map of W22 at 18 cm

A color composite image of the complex is shown in Figure 7.3. Numerous shells are seen in the image. Red, green and blue emissions are from [SII] $6716-31$Å, H_α and [OIII] 5007Å respectively. The singly ionized sulfur shows up well in areas

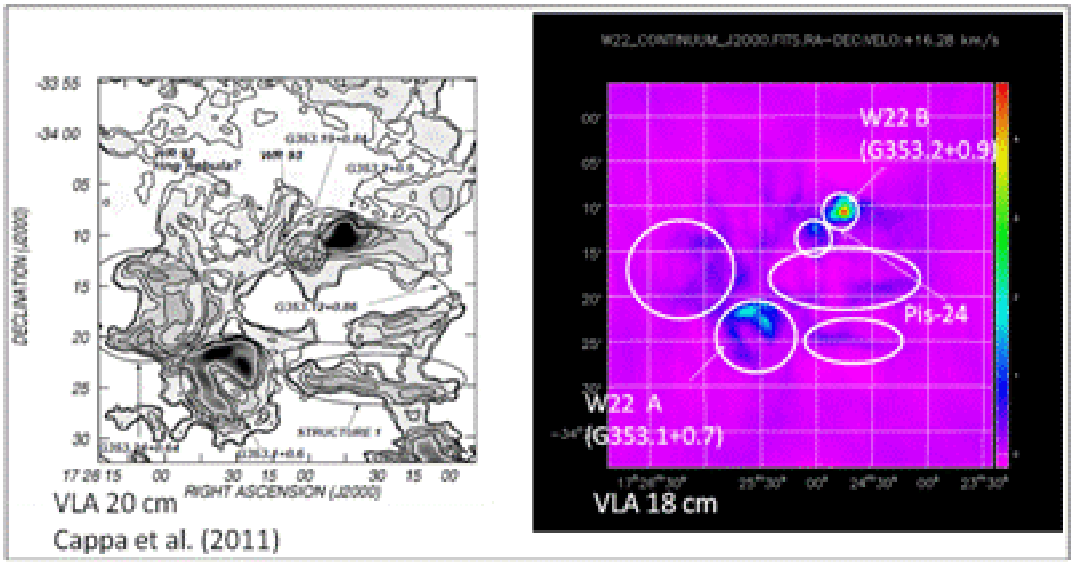

Figure 7.2: Comparison of two radio maps. Note that most of the prominent features coincide in the two images.

of compression, like where the expanding nebula hits the interstellar medium, which compresses the nebula. The H_α emission results when electron recombines with proton after hydrogen is being ionized. The electron subsequently cascades to the ground state and the transition from $n = 3$ to $n = 2$ gives H_α light. Therefore H_α emission traces ionized hydrogen and hence recent star formation. It can be seen that the bright regions in the VLA map coincide with the H_α emission, both coming from the ionized region. The [OIII] emission requires energy greater than 13.6 eV. The square shows the field observed with the VLA for our study. The large shell can be seen prominently but there is no [OIII] emission along the shell implying that this is a low excitation region. At -34^d18^m; 17^h24^m, a layer is seen in both radio and composite image. The winds from the stars in pismis-24 have cleared out the surrounding gas and dust, creating a void (a low density region) seen in the center of radio maps. The layer shows how far out the gas has been eroded. Hence, G353.12+0.86 is a stellar wind bubble. A region between the star cluster and the molecular cloud is zoomed in and shown in Figure 4.2. This image is taken by the HST-WFPC2 camera at 0.8 μm. A pillar like region is seen in the image at $17^h24^m45^s$, $-34^d10^m55^s$ (Figure 4.2). It is pointing towards Pismis-24 and its projected distance from it is ~ 3.5 pc (Westmoquette et al. 2009). The reason for its formation is that some sections of the original gas cloud are denser than the others, having more gas and hence more dust. As a result, the radiation from the surrounding stars is mostly absorbed by the dust and these regions are also able to resist the erosive power of stellar winds. Therefore such small regions of dense gas remain protected, leaving behind these gas pillars, also called as elephant trunks. High resolution optical/near IR IFU observations show that the gas on the pillars edge is denser, hotter, and more highly excited than its surroundings, which clearly suggests that the incoming radiation and winds

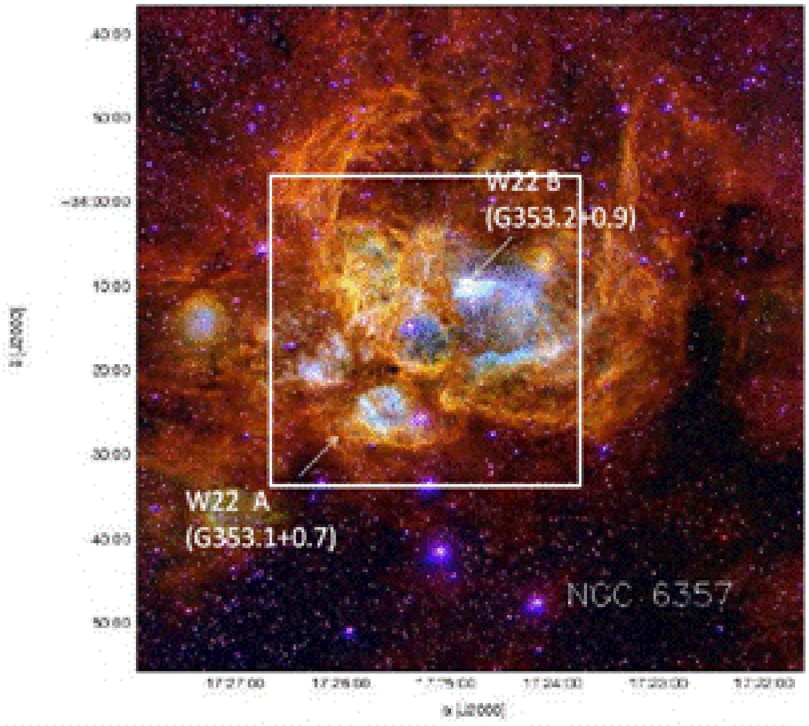

Figure 7.3: A color composite image obtained from CTIO Schmidt Camera (Cappa et al. 2011). The box shows the regions observed with the VLA for current study.

from the cluster stars are strongly affecting the state of ionized gas in these surface layers. This kinematical evidence of strong interaction between Pismis-24 and the gas in the trunk was provided by Wesmoquette et al. (2009).

Figure 7.4 is another infrared image of W22 complex obtained from SPITZER IRAC archive. The emission at $8\mu m$ features from Poly Aromatic Hydrocarbons (PAHs). These PAHs are important component of the interstellar dust. They do not survive in the H^+ regions but they do on neutral PDR at the interface between ionized and molecular gas. This image shows that PDRs are widespread in the complex indicating presence of neutral gas and it could be inferred that there is molecular gas present in the complex. It should be noted that the H_α emission coincides with the dust emission because the UV radiation heats dust which reemits at infrared wavelengths.

7.2 OH spectral line studies

In order to investigate the physical conditions in a star forming region, some physical parameters of the region, such as proton column density, internal velocity dispersion should be known. The OH velocity profiles are shown in Figure 7.5(a). A velocity component is seen at −5.6 km/s towards W22 B and another component at +5.8 km/s towards W22 A. The negative velocity absorption component is considered to be associated with the actual HII region based on CO emission lines and RRL observations (Figure 7.5(b), (c)); however, the component at +5.8 arises in a cold

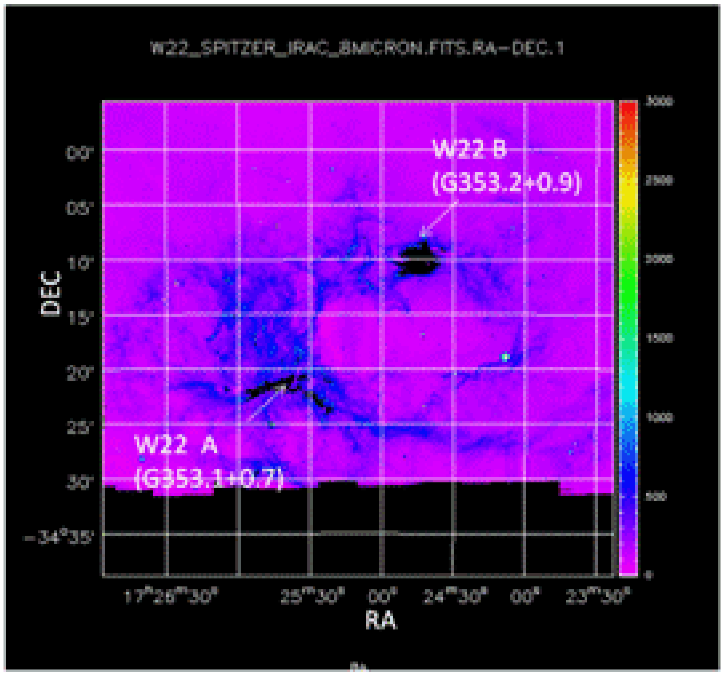

Figure 7.4: SPITZER-IRAC image at $8\mu m$.

Table 7.1: Observed features of line profiles

Source	Position		V_{LSR}		ΔV_{FWHM}	
	R.A. ($J2000$)	DEC ($J2000$)	km s^{-1}	km s^{-1}	km s^{-1}	km s^{-1}
W22 B	17h 24m 45.77s	-34d 10m 38.91s	-5.7	+5.0	2.2	0.6
W22 A1	17h 25m 26.91s	-34d 22m 58.96s	-5.1	+5.8	2.2	0.7
W22 A2	17h 25m 36.60s	-34d 21m 48.85s	-1.0	+5.6	1.6	0.6

cloud that is not associated with W22. This cloud was observed by Riegel & Crutcher in 1972 and its estimated distance is ∼ 150pc from the sun (Crutcher and Lien, 1984). The negative velocity components are single-peaked while the component at positive velocities are broad and show multiple peaks.

Optical depth profiles for OH 1667 MHz line can be calculated from the velocity profiles and are shown in Figure 7.5(b). The task COMB in AIPS was used to generate the optical depth profiles. The center velocities and line-widths are summarized in Table 7.1. The opacity in OH is very low towards W22 B, about 9% and that towards W22 A1 is 24%. The OH column density is determined using the relation (3.16) and the values are listed in Table 7.2.

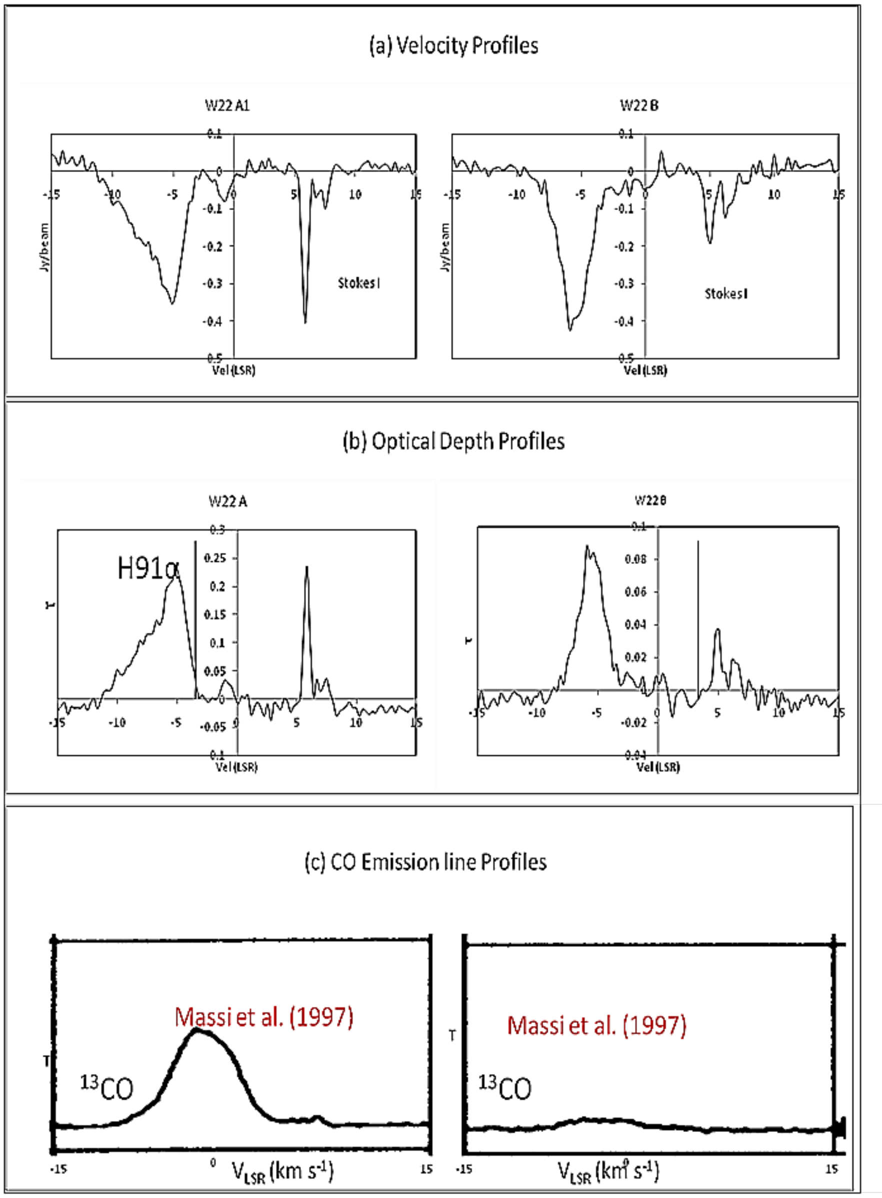

Figure 7.5: (a) Velocity profiles (b) Optical depth profiles (c) CO line emission profiles at two positions towards W22.

7.3 Magnetic fields

As explained in section(3.2.1) that if the Zeeman effect is present, then Stokes V profile will exhibit a scaled down replica of the derivative of the Stokes I line profile, with the amplitude of the derivative replica proportional to B_{los}. Figure 7.6 shows stokes I and stokes V profile at 2 positions i.e. W22 A1 and W22 B. However, we could not see an S curve at which there is absorption in I profile. Therefore, we could not detect magnetic field strength in either the local cloud or in a cloud associated with H^+ region in W22 due to high noise level.

Table 7.2: OH column densities

Source	Position		ΔV_{FWHM}	$N(OH)/T_{ex}$	N(OH) $\times 10^{13}$
	R.A. ($J2000$)	DEC ($J2000$)	km s^{-1}	$cm^{-2}\ K^{-1}$	cm^{-2}
W22 B	17h 24m 45.77s	-34d 10m 38.91s	2.2	5.07 $\times 10^{13}$	0.13
W22 A1	17h 25m 26.91s	-34d 22m 58.96s	0.4	2.31 $\times 10^{13}$	0.06
W22 A2	17h 25m 36.60s	-34d 21m 48.85s	3.8	5.07 $\times 10^{13}$	0.13

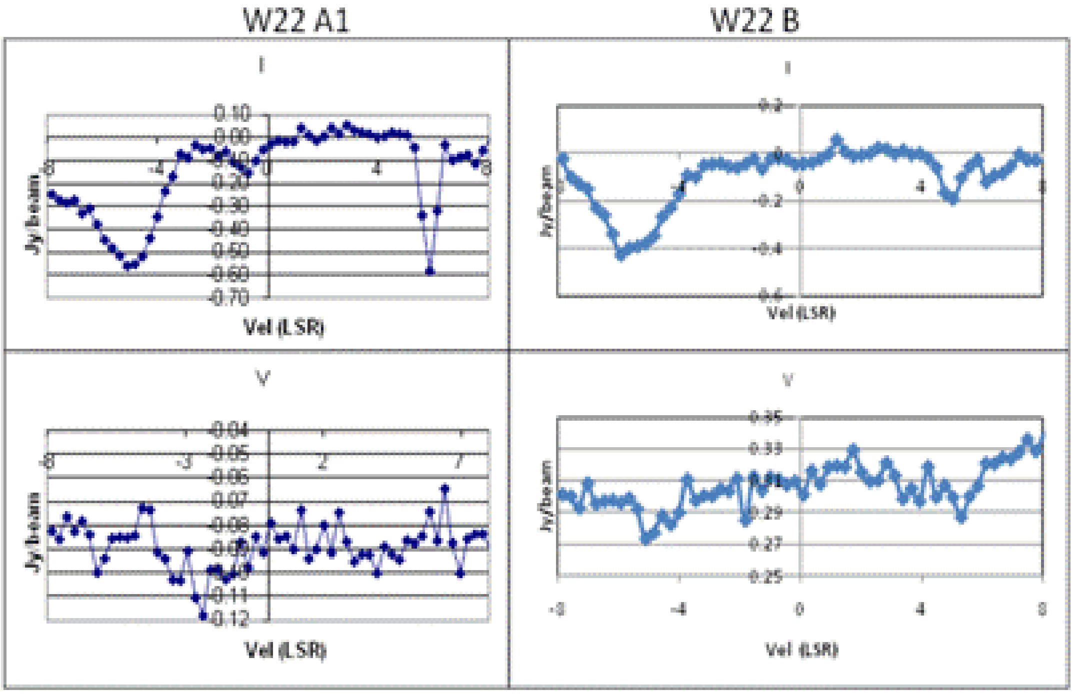

Figure 7.6: Stokes I and V profiles at W22 A1 and W22 B.

Chapter 8 Discussion

8.1 Physical Parameters of the Cloud

Zeeman effect measurements can be used to estimate the magnetic field strengths and other relevant physical parameters of the region. We have estimated the OH column densities from the molecular OH line data. The proton densities are calculated from OH column densities using the conversion ratio (3.17) and a summary of the measured physical parameters is listed in Table 8.1. The average values of proton column densities are compared with the values obtained from Russeil et al. (2010). Figure 8.1 shows H_α image of W22 with extinction contours overlaid on it. We have calculated the proton column density by determining the visual extinction at W22 A and W22 B and then using the relation (3.18). A_v was found to be 16.5 mag at both W22 A and W22 B positions. Using this conversion ratio, we obtain a value of $N(H_2) = 3.1 \times 10^{22} cm^{-2}$ for W22 A. Note that this value compares well with $N(H_2) = 2.7 \times 10^{22}\ cm^{-2}$ obtained from our observations. However the value $N(H_2) = 0.9 \times 10^{22}\ cm^{-2}$ obtained for W22 B is one third the value obtained from Russeil et al.(2010). The values of N(H) that we obtained are also comparable with N(H) estimated from CO emission lines by Massi et al. (1997). They obtained $N(H) \sim 10^{21}\ cm^{-2}$ for W22 A and $N(H) \sim 10^{22}\ cm^{-2}$ for W22 B.

The critical field can be estimated using a straightforward relation,

$$B_{crit} = 5 \times 10^{-21} N(H) \qquad \mu G \tag{8.1}$$

Where B_{crit} is the average magnetic field in a cloud that would support it against its own gravity. We found B_{crit} for the actual and local cloud towards W22 A and W22 B and the values are listed in Table 8.2.

The magnetic field for the local cloud at W22 A1 was found to be $\sim 20\ \mu G$ (Kazes and Crutcher 1986). Figure 8.2 shows OH 1667 MHz velocity profiles for (a)stokes

Table 8.1: Summary of measured physical parameters

Source	$N(OH)/T_{ex}$ kms^{-1}	τ_{max}	N(OH) cm^{-2}	N(H) cm^{-2}
W22 B	-5.7	0.09	2.0×10^{15}	8.0×10^{21}
	$+5.0$	0.04	0.2×10^{15}	8.0×10^{20}
W22 A1	-5.1	0.24	5.3×10^{15}	2.1×10^{22}
	$+5.8$	0.24	1.6×10^{15}	6.4×10^{21}
W22 A2	-1.0	0.05	0.8×10^{15}	3.2×10^{21}
	$+5.6$	0.23	1.4×10^{15}	5.6×10^{21}

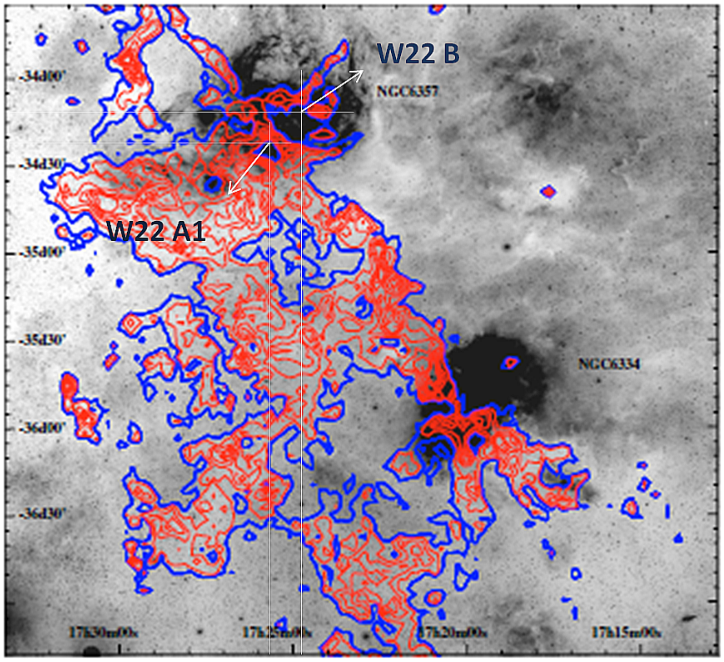

Figure 8.1: H_α image of W22 complex and its surroundings with extinction contours overlaid on it (Russeil et al. 2010).

Table 8.2: B_{crit} for W22

Source	V_{center} kms^{-1}	N(H) cm^{-2}	B_{crit} μG
W22 B	-5.7	8.0×10^{21}	40
W22 A1	-5.1	2.1×10^{22}	105

I; (b)stokes V and (c)scaled dI/dV for $B = 20\ \mu G$. The dotted line shows the exact position where the absorption is seen. It can be seen that the noise level in stokes V shown is higher than the expected amplitude shown in dI/dV. Figure 8.3 is similar to Figure 8.2 but the scaled dI/dV is for $B = B_{crit} = 105\ \mu G$ for the actual cloud at W22 A1. The red line shows that the amplitude of dI/dV is much lower than the noise level in stokes V profile. Hence the sensitivity of the array is insufficient to detect such low magnetic field strength. This could explain why we could not detect any magnetic field from our observations.

8.2 RRL Studies

We observed two different velocities of OH towards W22. It implies that two different molecular gas clouds are present along the line of sight. We inferred that the gas at positive velocities correspond to gas in a local cloud based on previous studies of the local cloud (Kazes and Crutcher, 1986) and our velocities are in agreement with them. The gas at negative velocities is certainly associated with the H^+ region in W22

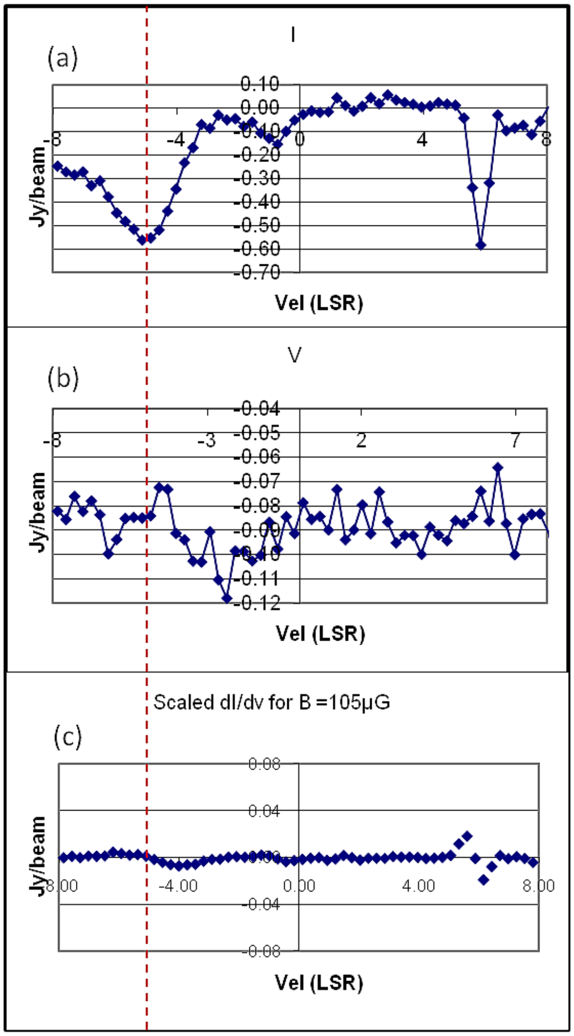

Figure 8.2: OH 1667 MHz velocity profiles for (a)stokes I; (b)stokes V and (c)scaled dI/dV for $B = 20\ \mu G$ at W22 A1 in the local cloud that is not associated with W22 complex.

because the radio recombination lines are observed only from ionized hydrogen region and all previous RRL studies show negative velocities towards W22. We compared the velocities of hydrogen and carbon recombination lines with OH velocities. Table 8.3 summarizes different velocities towards W22 complex. We have used data of $H109_\alpha$ from Wilson et al. (1970) and more recent observations of $H91_{alpha}$ and $C91_{alpha}$ from Quireza et al. (2006). Note that the hydrogen and carbon RRL velocities are comparable but all are lower than the OH velocities. This could be explained based on the fact that the radio recombination lines are emitted from the H^+ region and OH absorption is coming from the H_2 region.

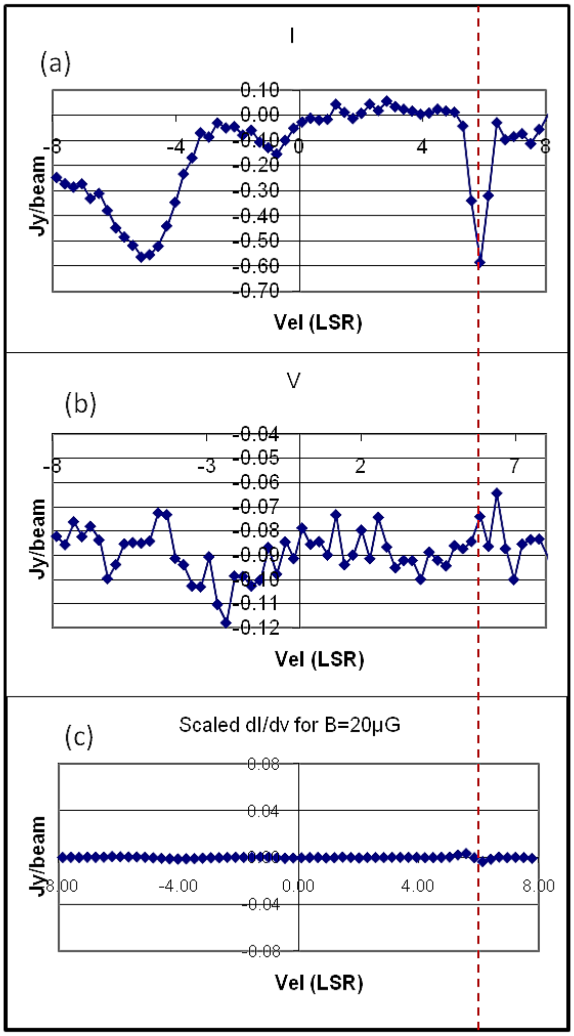

Figure 8.3: OH 1667 MHz velocity profiles for (a)stokes I; (b)stokes V and (c)scaled dI/dV for $B = 105\ \mu G$ at W22 A1 in the actual cloud that is associated with W22 complex.

Table 8.3: Summary of RRL velocities

Source	V_{LSR} km s^{-1}			
	$H109_{\alpha}$	$H91_{\alpha}$	$C91_{\alpha}$	OH
W22 A	-4.1	-3.8	-4.3	-5.1
W22 B	-3.8	-3.6	-4.3	-5.7

Chapter 9 Conclusions

We have observed the OH (1667 MHz) line in a galactic star forming region W22 to study the physical conditions in this complex. We searched for magnetic field strengths in both the clouds using the Zeeman effect. We could not detect magnetic field strengths in either the local cloud or in the cloud associated with the H^+ region. We compared stokes V profile with the scaled dI/dV profile at $20\mu G$ (measured from previous studies of W22 by Kazes and Crutcher, 1986) at the position W22 A. We also calculated the critical magnetic field strength in the actual cloud at W22 B to be $105\mu G$ and compared stokes V profile with the scaled dI/dV profile at B_{crit}. In both the cases, it was found that the noise level in stokes V profile is much higher than the expected amplitude. Therefore we conclude that the sensitivity of the VLA is insufficient to detect expected fields. We calculated the column density of OH in both the clouds and inferred proton column density N(H) from it. $N(H)_{tot} = N(H)_{localcloud} + N(H)_{actualcloud}$ compared well with N(H) inferred from visual extinction (A_v) observations (Russeil et al.2010) towards W22 A. For this comparison, we considered total N(H) because visual extinction observations at infrared wavelength does not separate the two gases at different velocities. This comparison implies that almost all of the ISM responsible for visual extinction must lie in front of the H^+ region since OH absorption only samples gas in front of the H^+ region. Therefore, we can conclude that the H^+ region may be a blister region on back side of molecular cloud towards W22 A. However, N(H) inferred from our observations was about one third of that inferred from A_v observations towards W22 B. Hence, only one third of the ISM responsible for A_v must lie in front of the H^+ region. And therefore, most of the molecular gas is located behind the H^+ region towards W22 B. The absorption lines thus reveal spatial structure in "local" H_2 gas (Riegel-Crutcher cloud) and in H_2 gas associated with the W22 region. Such observations are therefore useful in understanding the nature and structure of star forming regions and how they evolve with time.

Bibliography

[1] Bohigas J., Tapia, M., Roth M., Ruiz M. T., 2004, AJ,127, 2826.

[2] Brogan C., Troland T.H., Crutcher R.M., 1999, AJ,127, 2826.

[3] Burke B. F., Graham-Smith F., 1997, An Introduction to Radio Astronomy, 2nd Ed., Cambridge University Press: Cambridge.

[4] Cappa C.E., Barba R., Duronea N.U., Vasquez J., Arnal E.M., Goss W.M., Fernandez Lajus E., 2011, MNRAS, Volume 415, Issue 3, pp.2844-2858.

[5] Chaisson 1974, AJ, 79, 555.

[6] Crutcher 2007, EAS Publications Series, Volume 23, 2007, pp.37-54

[7] Crutcher R. M., Hakobian N., Troland T. H., 2009, ApJ, 692: 844.

[8] Elitzur M. 1991, Astronomical Masers, Kluwer Academic Publishers.

[9] Felli M., Persi P., Roth M., Tapia M., Ferrari-Toniolo M., Cervelli A., 1990, AA, 232, 477.

[10] Healy K., Hester J., Claussen M., 2004, ApJ, 610, 835.

[11] Heiles C., Stevens M., 1986, ApJ, 301: 338.

[12] Kazes I., Crutcher R. M., 1986, AA, 164, 328.

[13] Crutcher R. M., Kazes I., Troland T. H., 1987, AA, 181, 119.

[14] , High Energy Astrophysics, 2nd Ed., Cambridge University Press: Cambridge.

[15] Lortet M. C., Testor G., Niemela V., 1984, AA, 140,24.

[16] Lykins, Matt, "PHYSICAL CONDITIONS INCLUDING MAGNETIC FIELDS IN SEVERAL STAR FORMING REGIONS OF THE GALAXY" (2010). Doctoral Dissertations. Paper 95., http://uknowledge.uky.edu/gradschool$_diss$/95.

[17] Massey P., DeGioia-Eastwood K., Waterhouse E., 2001, AJ, 121, 1050.

[18] Massi F., Brand J., Felli M., 1997, AA, 320, 972.

[19] Matsuura M., Zijlstra A.A., Gray M.D., Molster F.J., Waters L.B.F.M., 2005, AIP Conference Proceedings, Volume 804, pp. 212-213.

[20] McBreen B., Jaffe D. T., Fazio G. G., 1983, AJ, 88, 835.

[21] Munoz D., Mardones D., Garay G., Rebollido D., Brooks K., Bontemps S., 2007, ApJ, 668, 906.

[22] Neckel T., 1978, AA, 69, 51.

[23] Quireza C., Rood R. T., Bania T. M., Balser D. S., Maciel W. J., 2006, ApJ, 653, 1226.

[24] Palmer P., Zuckerman B., Penfield H., Lilley A.E., 1969, ApJ,156, 887.

[25] Persi P., Ferrari-Toniolo M., Roth M., Tapia M., 1986, AA, 170, 97.

[26] Rohlfs K., Wilson T. L., 2006, Tools of Radio Astronomy, 5th Ed., Springer: Berlin.

[27] Russeil D., Zavagno A., Motte F., Schneider N., Bon-temps S., Walsh A. J., 2010, AA, 515, A55.

[28] Rybicki G. B., Lightman A. P., 1979, Radiative Processes in Astrophysics, Wiley: New York.

[29] Sakellis, S., Taylor, M. I., Taylor, K. N. R., Vaile, R. A., Han, T. D., 1984, PASP, 96, 543.

[30] Sarma A. P., Troland T.H., Roberts D. A., Crutcher R. M.,2000, ApJ, 533:271.

[31] Schraml, J., Mezger, P. G.,1969, ApJ, 156, 269.

[32] Slysh V. I., 1974, Astron. Zh., 51, 912.

[33] Troland T. H., 1990 Proceedings of the 140th Symposium of IAU, Heidelberg, Federal Republic of Germany, June 1989, Dordrecht, Netherlands, Kluwer Academic Publishers, 1990,p. 293-300.

[34] Wang, J., Townsley, L. K., Feigelson, E. D., Getman, K. V.,Broos, P. S., Garmire, G. P., Tsujimoto, M., 2007 ApJS,168, 100.

[35] Westmoquette M.S., Slavin, J.D.,Smith, L.J., Gallagher III, S.J., 2010, MNRAS, 402, 152.

[36] Wilson, T. L., Mezger, P. G., Gardner, F. F., Milne, D. K., 1970, AA, 6, 364.

Vita

Akshaya Rane

Date of birth:

April 23^{rd}, 1984

Place of birth:

Mumbai, India.

Educational Institutions attended and degrees awarded:

University of Mumbai, M.S. 2006

Professional positions held:

Project Assistant for International Astronomy Olympiad, HBCSE, Tata Institute of Fundamental Research, Mumbai, 2007-2008

Graduate Teaching Assistant, University of Kentucky, 2008-2010

Scholastic and professional honors:

Recipient of University of Kentucky Huffaker Travel Grant, 2010

Ranked 1^{st} in the B.S. (Physics) Examination, K. J. Somaiya College of Arts and Science, 2004.